Nuclear Instruments and Methods in Physics Research A 1062 (2024) 169226

Contents lists available at ScienceDirect

Nuclear Inst. and Methods in Physics Research, A

journal homepage: www.elsevier.com/locate/nima

Calibration-free 3D ray-tracing beam hardening correction in computed tomography

Marco Seracini [a,b], Matteo Bettuzzi [a,b], Rosa Brancaccio [a,b,*], Maria Pia Morigi [a,b]

[a] Department of Physics and Astronomy "Augusto Righi", University of Bologna, Viale Berti Pichat, 6/2, Bologna, 40127, Italy
[b] National Institute for Nuclear Physics, Section of Bologna, Viale Berti Pichat, 6/2, Bologna, 40127, Italy

ARTICLE INFO

Keywords:
Beam hardening correction
Cone-beam geometry
Computed tomography
Imaging

ABSTRACT

In this paper we introduce a calibration-free beam-hardening correction technique in computed tomography, which improves the results achieved by a state-of-the-art correction method. Two main practical points are here underlined: (1) the need to perform a beam hardening correction without previous calibration; (2) the need to consider the shape of the object in all its whole three-dimensional extent. The proposed method requires: (a) a first complete reconstruction of the object by means of a cone-beam filtered back projection algorithm; (b) a segmentation of the reconstructed volume; (c) the construction of the attenuation when varying path-length graph; (d) the interpolation of the experimental data on the graph with a convenient mathematical function; (e) the correction of the measured attenuation values; (f) to perform again the complete cone-beam reconstruction. The result is an effective beam-hardening calibration-free correction over a large variety of objects, easy to use and quite fast. The proposed method results particularly useful when both the measurement time and the control of the geometry of the system are limited, like the ones generally faced in Cultural Heritage diagnostics. Computed Tomography reconstructions for test samples and for real cases are provided to highlight the effectiveness and the advantages of the new suggested approach.

1. Introduction

Computed Tomography (CT) is a consolidated technique allowing to reconstruct a 3D virtual model of the object under investigation by means of multiple projections from different observation angles. The goal of CT imaging in Cultural Heritage (CH) [1–3] is to achieve a three-dimensional representation of the object under investigation. This outcome is of great importance both from a historical perspective, to study the construction techniques of the artworks and to provide restorers with information about their state of conservation. Last but not least, the reconstructed volume can serve as the foundation for the virtual exploration and the creation of Digital Twins in CH [4].

In this work we focus on X-ray CT, Filtered Back Projection (FBP) based reconstruction [5], which employs radiation sources to perform attenuation measurements. The attenuation values depend on different physical parameters: the length of the path crossed by the X-rays; the density distribution and the atomic number of the object; the energy of the X-ray beam.

Generally, the used X-ray tube emits a polyenergetic beam, giving reason to a distributed energy spectrum (in keV for each specific tube). Neglecting this frequency distribution causes undesired artifacts: a typical one is represented by the so called "cupping effect", that occurs when a homogeneous material layer, characterized by density and composition giving a constant linear attenuation coefficient (in a logarithmic scale), is instead typically reconstructed with a radial gradient decreasing towards the centre of the object (see Fig. 1). This class of artifacts is due to different attenuation rates of low and high energy photons, such that the average beam energy increases with the penetration depth through the material. The correction of these artifacts, due to the X-ray beam hardening, is generally referred to as Beam Hardening Correction (BHC). It is possible to narrow to some extent the energy spectrum range by means of filtration with metal layers positioned at the output of the source (the so-called filters) or using particular dual or multi energy-selective detectors. However, these hardware solutions still have physical limitations (an ideal monochromatic spectrum cannot be achieved), and it also significantly reduces the intensity of the incident beam, resulting in noisier images or longer acquisitions, making it not always a practical choice.

In the literature, different techniques for the BHC have been proposed.

* Corresponding author. Department of Physics and Astronomy "Augusto Righi", University of Bologna, Viale Berti Pichat, 6/2, Bologna, 40127, Italy
E-mail address: rosa.brancaccio@unibo.it (R. Brancaccio).

https://doi.org/10.1016/j.nima.2024.169226
Received 7 August 2023; Received in revised form 9 February 2024; Accepted 29 February 2024
Available online 6 March 2024

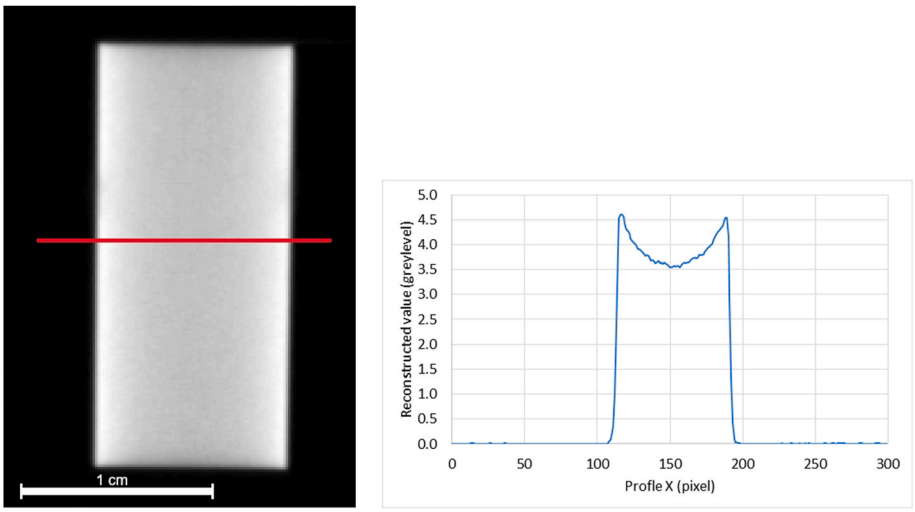

Fig. 1. Typical beam hardening artifact: cup-shaped trend of the intensity in case of a homogeneous 1 cm diameter aluminium cylinder. In (a) a reconstruction on the transversal plane; in (b) the profile of the grey levels on the reference red line plotted in (a).

From one hand, exploiting a formal physical/mathematical formalization, it has been seen that a bimodal energy model for the detected energy spectrum can be used for BHC in well-specified conditions [6,7]. On the other hand, in presence of considerable data amount, the need for a reduced time to set up the experiment and to compute the reconstruction, makes the proposed solution not acceptable in some real cases. For these reasons, more experimental-oriented methods have been introduced and proved to be effective, even if mostly validated on experimental results.

To perform the BHC, techniques employing physical prefiltration with metal filters are available. In this kind of techniques metal layers of opportune material (e.g., aluminium, copper) and thickness are inserted before the measurement stage to harden the beam [8–10]. This method is effective especially when the internal structure of the object under investigation is known, as it happens in the medical CT. In the CH context, this approach is not always viable, due to the unknown internal structure and composition of the artifacts and to the limited available time for the acquisitions.

Other BHC approaches use phantoms, i.e., ad hoc built specimens: they are employed to experimentally determine the detector calibration curves for specific materials, such that the correction can be propagated to the acquired data [11–13]. This technique is mostly used for water beam hardening correction, generally useful for medical scans. Again, the difficulties to apply this class of techniques to the CH context reside in the unknown internal structure and material of the artifacts.

The last group of BHC techniques involves the introduction of image-content based techniques [14–18].

In this case, the acquired CT projections are used to achieve a first estimate of the material composition and of the measurement errors due to beam hardening artifacts. Subsequently, the identified errors are compensated on the acquisition data, such that the final reconstructions will appear beam hardening corrected. The BHC method that we propose in this work belongs to this class of algorithms.

Other image-based techniques have also been proposed to attempt the BHC of multi-material objects: in these cases, image processing algorithms are used to individuate homogeneous zones inside the virtual object reconstruction and then the correction is operated for each single uniform area [19]. The application of this class of methods is strongly connected to the efficiency of the segmentation algorithm. In the CH context, the segmentation of different structures can be difficult, and, in some cases, the extent of the homogeneous area can be large enough, such that problems of saturation can corrupt the final reconstructions (see, e.g., Fig. 12). Therefore, a mathematical model able to face these situations is needed.

Once again, we highlight how in the context of Cultural Heritage CT scans, objects under examination are often made up of inadequately characterized materials. As a case study, this article examines Canova's sketches. Canova models are primarily composed of terracotta or plaster, materials that currently exhibit uncertainty in purity and concentrations and that evolved over the years due to natural degradation. Consequently, the use of a contemporary terracotta or plaster phantom for beam hardening analysis could be both misleading and expensive in terms of time and costs. Moreover, CH works can be fashioned from a variety of materials, including different types of wood, ceramics, clay, marble, and more. Phantoms must not only replicate the original state of the object but also its current condition, which can impact density and chemical-physical properties. This wide range of materials and dimensions needs the selection of different beam energies and, consequently, various acquisition components, such as X-ray tubes with different focal spots, currents, and distinct detectors.

Hence, in this context, the creation of a dedicated phantom for each individual object is indeed impractical. This is why a flexible calibration free BHC tool that can be applied post-acquisition is needed.

Differently from the medical case, in CH there is no issue related to radiation dose. Extensive studies have shown that X-ray tomography analysis does not alter the material properties because it does not involve living organisms [20–22]. The only known case of damage is that of amber and glass, which may experience yellowing but can be reversed with mild heating of the artifact [23]. Radiation damage effects, on the other hand, have been observed at high beam intensities [24] and elevated energies beyond the power of the common X-ray tubes used in this study.

On the other hand, our research group conducts in situ CT analyses. This involves transporting the equipment to the museum and restricting visitors access to certain areas, as well as the privation to exhibit the artworks under examination for the entire duration of the analyses. Additionally, large artworks like statues require multiple scans from various angles to achieve higher resolution over multiple sections of the same work. As a result, for each sizable object, the acquisition time multiplies by the number of sections necessary for a comprehensive scan (In some cases, we acquired up to thirty thousand radiographs for each object).

In addition, the cost of the equipment, the transportation, and the stay in the museum is substantial, being these analyses often funded by limited budgets. Then, it is evident that reducing the investigation time is of the greatest importance. Fixed the campaign duration, the goal

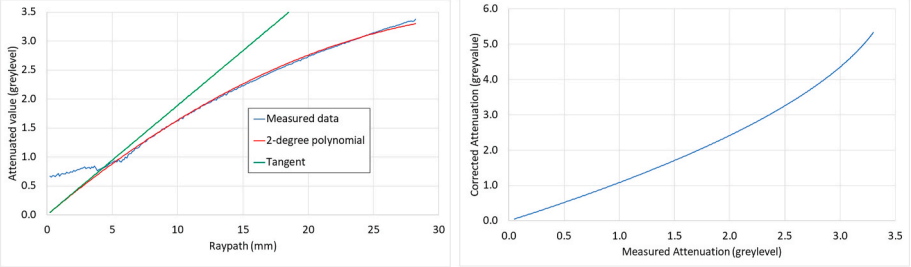

Fig. 2. (a) in blue, the data obtained from ray-tracing on the central slice, in red the second-degree polynomial fit, and in green the tangent at the origin of the polynomial. (b) The correction curve calculated using the formula (6).

usually is to analyse as many artworks as possible. Then, a saving-time calibration-free method for BHC appears to be the best suitable solution in the CH scenario.

To speed up the procedure, among BHC methods which are calibration-free (e.g., Refs. [12,14,25]), we decided to follow the approach of Zhao et al. [26] because of its experiment-related nature. The method is based on real uncorrected CT data, used to build the X-ray attenuation when varying the path-length graph on which the correction is then calculated. The proposed technique has been successfully applied, e.g., to the micro-CT analysis of small lead spheres of archaeological interest [27]. However, the proposed approach of taking into consideration just the central slice of one object (the only one that can be correctly reconstructed with a fan-beam FBP algorithm) appears soon inadequate when objects of more complex shapes are scanned with a cone-beam CT system (kind of objects that are easily found in CH). For these reasons, in this paper we introduce an extension of the method proposed by Ref. [26]: a ray-tracing algorithm calculates the X-ray path-length through the object in 3D and it puts them properly in relation with the measured attenuation values.

Moreover, after the positioning of the mobile in-situ system, to avoid photon starvation and saturation, some fast tests for the setting of the acquisition parameters are performed on representative given artifacts. Even if the two phenomena are opposite, the setting of the acquisition parameters is made to have on the detector the best possible level of signal for the acquisition. This operation guarantees that, in most cases, the acquired images have enough level of contrast and that the dynamic range of the detector is fully exploited.

Differently from Ref. [26], our method suggests managing the BHC by the introduction of two different regions of correction, depending on the ray-path length: for high values of it, our "far field" approximation avoids saturation in the final reconstructions. Moreover, we perform preventive volumetric analysis to heuristically tune the model with a suitable numerical value to bound the two approximation regions.

The proposed method requires: (a) a first complete reconstruction of the object by means of a cone-beam Feldkamp (FDK) algorithm; (b) a segmentation of the reconstructed volume based on a threshold that has to be carefully evaluated; (c) the construction of the graph of the attenuation as a function of path-length; (d) the interpolation of the experimental data on the graph with a convenient mathematical function; (e) the correction of the measured attenuation values to match a Beer-Lambert type pure exponential law; (f) to perform again the complete cone-beam FPB reconstruction of the object.

The method proposed in Ref. [26] bases its efficacy on implicit assumptions on the shape and structure of the object, being strictly valid only when two conditions are met:

- central symmetry;
- homogeneity in the constructive material.

Both of the previous conditions are not feasible in most real cases. If a certain degree of symmetry can be assumed for industrial parts, this assumption is commonly not true for CH objects (see, e.g., Ref. [28]), which, on the contrary, are characterized by the irregularity of their shape and the inhomogeneity of their construction materials, as can be observed in the case of the two Canova's sketches illustrated in Sec. 3.

Moreover, the method proposed in Ref. [26] considers only the mid-plane (CRS) of the source-object-system to be representative of the whole dataset: the CRS is then employed to generate the correction polynomial model. Again, this condition is far to be respected if the object is strongly asymmetrical.

For these reasons a more accurate modelling is desirable, and it is proposed in Sec. 2.

Moreover, to evaluate the quality of the BHC, achieved by the new proposed model, we extended it to complex cases in the CH context, for which the time available for in situ measurements is limited and the dataset of a single acquisition can amount to tens (sometimes hundreds) of Gigabytes.

In the following, the mathematical model is the core of Sec. 2.1, while in Sec. 2.2, Sec. 3.1 and Sec. 3.2 the software implementation and the associated results are respectively discussed. A conclusive paragraph summarizes the advantages of the proposed method.

2. Methods

2.1. Mathematical model

The cause of the beam hardening stands in the polyenergetic nature of the X-ray beam generally employed for CT scanning. The X-ray attenuation is modelled by the well-known Lambert-Beer law:

$$I = I_0 e^{-\int \mu(E,\rho,Z)dr} \tag{1}$$

where I is the measured intensity, due to the presence of the object, I_0 is the beam intensity, measured in absence of the object, μ is the linear attenuation coefficient and r is the X-ray path length. The linear attenuation coefficient μ depends on the object density ρ, the atomic number Z, and on the energy spectrum E emitted by the tube, such that this dependency can be explicitly expressed as μ(E,ρ,Z).

Starting from equation (1), the attenuated radiograph A(r) can be defined as follows:

$$A(r) = -\ln\left(\frac{I}{I_0}\right) = -\int \mu(E,\rho,Z)dr\,. \tag{2}$$

Attenuated radiograph is then directly proportional to the sum of the attenuation contributions along the path through the object. If the beam were monochromatic, the relationship between A(r) and r would be linear (in a logarithmic scale); however, in the real case, as the beam passes through the object, the less energetic component is attenuated, and the average energy of the beam increases. The subtraction of less energetic photons from the beam is higher as the ray-path through the object increases. Consequently, the values of A(r), acquired from longer ray-paths, decrease, being obtained by a more energetic, 'hardened', beam: this phenomenon is referred to as Beam Hardening. Experimentally, what is measured, when computing the values of each pixel in the

attenuated radiographs for each angle as a function of ray-paths through the object, is a curve that, for high values, deviates from the theoretical straight line, as illustrated in Fig. 2. This is the cause of the cupping effect shown in Fig. 1

The approach of Zhao et al. [26] is to perform a polynomial fit A′(r) of the experimental data A(r) in the central slice of the tomography. The N order fit can be expressed as follows:

$$A^{'}(r) = \sum_{n=1}^{N} C_n r^n \tag{3}$$

where C_n are the coefficients of the N order polynomial and $C_0 = 0$ because when the ray-path is equal to zero the attenuation should be null. Regardless of the chosen polynomial order, the theoretical line representing the correct relationship between attenuated radiograph and ray-path is determined by the tangent f of polynomial (3) calculated at the origin, taking the following form:

$$f(r) = C_1 r \tag{4}$$

Once C_1 has been experimentally determined, it is then possible to correct the attenuated radiographs at each angle by calculating, for each pixel, the respective ray-path through the object and replacing the measured value with the one obtained from the formula (4). In Ref. [26], the authors experimented their solution using both N = 4 and N = 2. The choice for N = 4 has been experimentally determined and its correctness seems to vary from case to case: in Refs. [29,30], where human thorax phantoms are employed, the author claims that the second order is enough to achieve opportune corrections and moreover, he underlines how higher values for N do not provide appreciable improvements.

Summarizing the details, the procedure described in Ref. [26] needs that the analysed object is firstly 3D reconstructed, then a segmentation is operated, using the Otsu method [31] and the Canny operators [32], and finally a correction to the data is applied. This correction is calculated considering the tangent f(r) to A'(r) in the origin, i.e., where the attenuation of the low energy component of the beam has not occurred yet (or, at least, it is negligible), thanks to the reduced r. The procedure is computed point by-point and only the central slice is considered to calculate the correction values (see Fig. 2).

This approach is not particularly convenient in case of a large amount of data, because the individuation of the ray-path for each data of each A(r) can be computationally demanding. For this reason, we introduce a new approach that drops the dependency from r and directly calculates the corrected value A*(r) from the experimentally measured value A(r), assuming a polynomial trend of order 2, obtaining r(A*) from (4) and replacing it in (3):

$$A(A^*) = C_2\left(\frac{A^*}{C_1}\right)^2 + C_1\frac{A^*}{C_1} \tag{5}$$

Inverting (5) we obtain:

$$A^*(A) = \frac{-1 \pm \sqrt{1 + \frac{4C_2 A}{C_1{}^2}}}{2C_2/C_1{}^2} \tag{6}$$

where the negative solution has not physical meaning. This substitution allows to work directly on the acquired intensity values in the correction step, without the need to calculate the ray paths and the corrections point-by-point through the volume, thus reducing the execution time.

Even if the introduced approximation is not generally valid from a theoretical point of view, it can be assumed to be acceptable when the different layers constituting the scanned object are each one internally quite homogeneous, behaviour that normally occurs in real experimental cases.

An example of data acquired experimentally by ray-tracing in the central slice, polynomial fit A'(r), and tangent f(r) is shown in Fig. 2 (a), while the results after correction are shown in Fig. 2 (b).

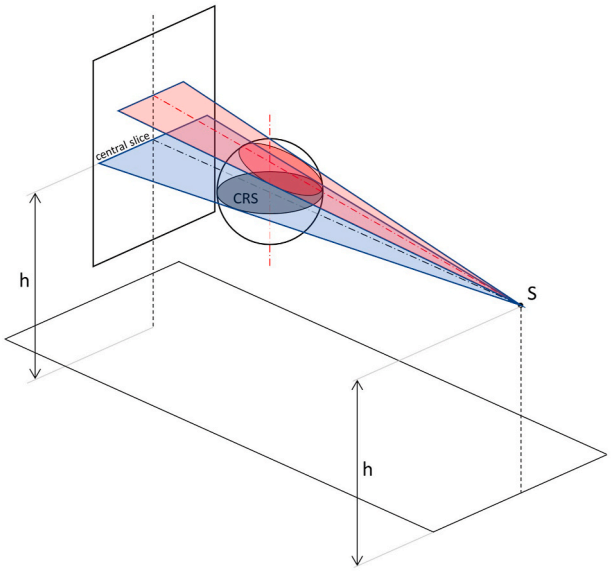

Fig. 3. Scheme of the fan geometry investing the object O (a sphere in this case). In blue the central slice individuated on the detector at the height h of the source S, respect to the ground plane. Highlighted in grey the Central Reconstructed Slice (CRS) while in red an example of a fan not passing for the central slice.

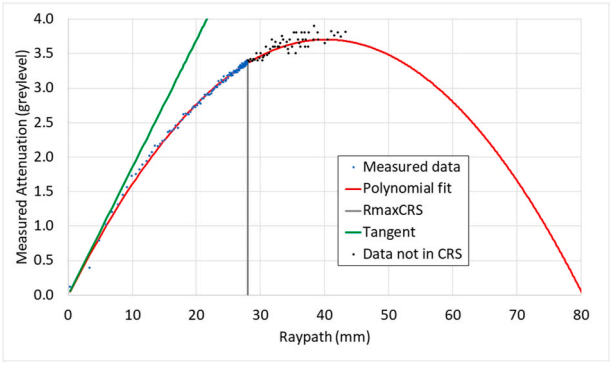

Fig. 4. In red, the polynomial function A′(r) (here N = 2) fitting the experimental data available in the CRS (in blue). In green the tangent to A′(r) in the origin. Measurement data are available, in the CRS only for $r \in [0, R_{maxCRS}]$, where $R_{maxCRS} = \max_{r \in CRS}\{r\}$. All the black points (i.e., outside the CRS, but anyway present somewhere in the object volume) are prone to over correction: in this example only the ones belonging to the area with r > 40 mm.

The solution proposed to solve the BHC problem approximating the trend of the CRS with A′(r) is not effective in complex cases. In presence of a cone beam geometry (see Fig. 3) the usage of the CRS as reference to calculate A'(r) is not enough accurate, with the risk that the CRS may not contain X-ray paths representative of the object under study. In fact, it could only contain a region with very long or very short paths when the object has a highly irregular shape, as in the case of a statue. Another common cause of polynomial approximation failure is represented by data exhibiting significant statistical fluctuations in the region corresponding to high attenuation and long ray-paths through the object. In this region, the signal is so high that it approaches saturation, and as a result, the polynomial fit may yield a curve with a maximum before the actual maximum path length, which clearly does not make sense from a physical point of view (attenuation cannot decrease with longer paths). When the data fit does not represent a correct physical trend, applying the proposed formula (6) results in an undesired over-correction in the region beyond the maximum in the fit. In summary, the cause of failure

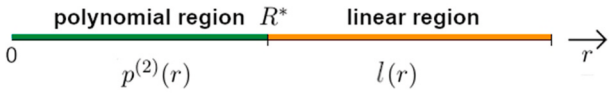

Fig. 5. Regions of approximation for the proposed model, when varying r. From left to right: in green the N-order polynomial approximation region, in orange the linear trend approximation region.

can be summarized in the following reasons:

- whatever A′(r), with N > 1, is not monotonic but exhibits maxima and minima points (their number depending on N and on its coefficients);
- the CRS does contain nor all the reconstructed attenuation values of the object, nor all the possible r, but only a subset of them both.

To overcome these problems, we propose a new mathematical model for calculating the correction of attenuated radiographs and the implementation of ray-tracing in 3D.

As shown in Fig. 4, if the maximum M of A'(r) is such that M > RmaxCRS, where RmaxCRS is the maximum thickness available in the CRS, the operated correction tends to increase in a not acceptable way (see the area for r > 40 mm in Fig. 4 again).

Moreover, when varying r, two cases can occur to the higher energy components of the beam after the filtering of the lower energy ones:

- they tend to pass through without any meaningful alterations of the average energy of the beam;
- they are completely attenuated.

This last behaviour expresses a stabilization of the phenomenon when increasing r, such that A(r) does not decrease anymore with r.

In Fig. 4, a typical trend of the measured data is shown: the measurements can be grouped in two main regions, one with a polynomial character (on the left of the graph) and the other one where a saturation occurs (on the right of the graph). Starting from this consideration, we propose a new attenuation model, in a different management of the points belonging to these two different regions, the limit separating them being indicated by R* (Fig. 5).

We formalize the new model as:

$$A'(r) = \begin{cases} p^N(r) & if \quad r \in [0, R^*] \\ l(r) & otherwise, \end{cases} \tag{7}$$

where $l(r) = ar + b$ expresses the tangent line to $p^N(r)$ in R*. If we assume N = 2 and $p^2(r) = k_2r_2 + k_1r + k_0$, we can explicitly calculate the values of a and b as:

$$a = 2k_2R^* + k_1, \quad b = -k_2R^{*2} + k_0 \tag{8}$$

In what follows, we will refer to the model formalized in (7) using the expression "mixed model", to distinguish it from the standard polynomial one.

Table 1
Values of the coefficients for the second and fourth-degree polynomials and the correlation coefficient for the data in Fig. 6.

	Cylinder 3 cm		Canova's statue	
Polynomial degree	2	4	2	4
C_0	0.00 ± 0.02	0.000 ± 0.017	0.000 ± 0.019	0.000 ± 0.006
C_1	0.19 ± 0.02	0.269 ± 0.017	0.027 ± 0.019	0.034 ± 0.006
C_2	−0.00 ± 0.02	−0.017 ± 0.017	0.000 ± 0.019	0.000 ± 0.006
C_3		0.001 ± 0.017		0.000 ± 0.006
C_4		0.000 ± 0.017		0.000 ± 0.006
R^2	0.988 ± 0.001	0.9921 ± 0.0008	0.85 ± 0.01	0.783 ± 0.005

For the "mixed model," we can also invert the equations to directly calculate the correction A* as a function of A, as we did in equations (5) and (6), and we can obtain the correction A*(A) even for r > R*, as shown in (9):

$$A^*(A) = \frac{k_1A - b}{a}; \text{ for } r > R^* \tag{9}$$

What has been achieved so far has been explicitly calculated for the second-degree polynomial and under the assumption that the tangent to the curve passes through the origin. However, it can be readily applied, with the appropriate mathematical modifications, also for higher-degree polynomial fit.

Approximations have been calculated for both N = 2 and N = 4 when r < R* and the results are shown in Fig. 6 and in Table 1. As can be seen from Fig. 6 there is no meaningful improvement between the second and the fourth order polynomial fit: the values of the coefficients are indicated in Table 1. The values of the Pearson Coefficient R^2 show how in the case of the cylinders the fits are equivalent while, in the case of a not homogeneous sketch the second order polynomial better correlates with the experimental data.

The new model is able to manage the data avoiding saturation in what we individuated to be the linear region. In particular we recall that, being the attenuation plotted in a logarithmic scale, the used approximation is, in effect, logarithmic: it is well known as many other physical phenomena involving saturation are realistically described by logarithmic/exponential trends.

We put in evidence that it is not possible to a priori calculate the value of R* but it needs to be experimentally determined and it strongly depends on the particular case. A first estimate can be performed assuming that R* must be contained in a neighbourhood of the maximum of p^N, i.e., R* ≤ M (see Figs. 6 and 7). The value of R* can be determined in a single approximation phase, given that all the data in the volume are available, differently from what happens in the CRS case.

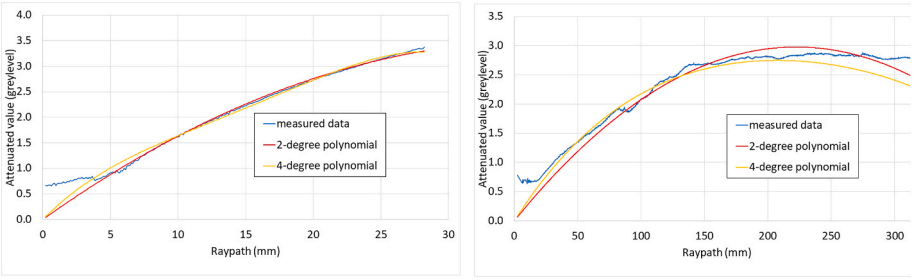

Fig. 6. Experimental data and the two polynomial fits for (a) a 3 cm cylinder and (b) a Canova's sketch. The fourth-degree polynomial does not improve the data fit for the 3 cm cylinder (a) while it worsens in the case of non-symmetric data from a Canova's statue affected by saturation (b).

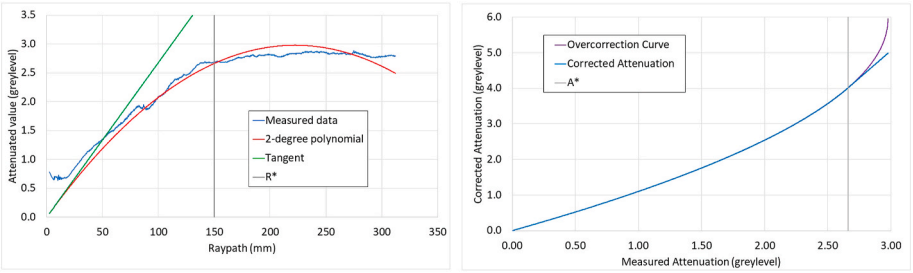

Fig. 7. (a) data obtained by computing the values of the attenuated radiographs as a function of the ray-paths, polynomial fit, tangent to the origin. (b) In violet, the correction curve calculated following [26]; in blue the one achieved using the mixed model.

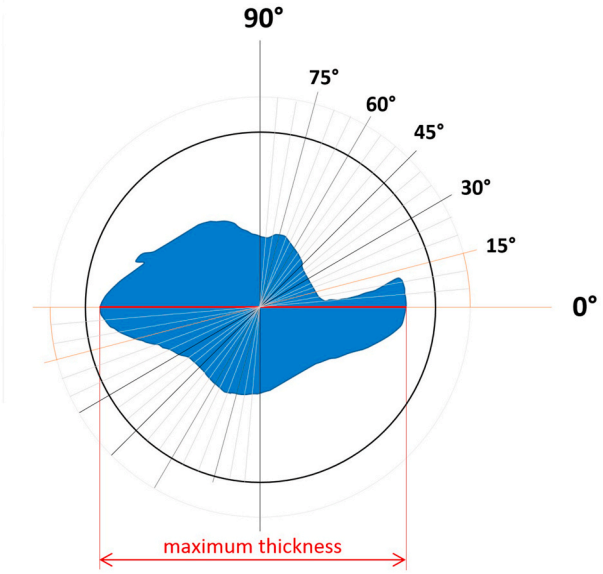

Fig. 8. Scheme of ray-tracing under 90° viewing angle. Each ray represents one of the 18 directions along which the 3D ray-tracing is performed. In this case the maximum thickness is found at the zero angle as the object is properly positioned.

Then, the new proposed mixed model completes the polynomial one, expanding the field of applications of the BHC to more complex cases.

2.2. Reconstruction software

An important aspect, when working with huge amount of data, as it is frequent in the CH field, is the computational cost of the used algorithms.

In this work, for the 3D object reconstructions, the proprietary software developed at the Department of Physics and Astronomy "Augusto Righi" of the University of Bologna and called PARREC (PARallel REConstruction) has been used (see, e.g. Refs. [33–35,36] for further details). PARREC uses an FBP approach to perform the 3D reconstructions, exploiting the CPU parallelization.

PARREC is implemented in C, importing the MPICH2 and National Instruments libraries. It is a graphical, interactive, and parallel software that can run on both regular computers and computer clusters [36]. In our case, the choice of using CPUs instead of GPUs is determined by two main reasons: the need to frequently move gigabytes of data and the possibility of integrating instrument acquisition and control tools. In fact, it is well known that GPUs offer significant computational power, but it is equally well known that there is a bottleneck due to data loading and unloading [37], operation that is particularly frequent during the CT reconstruction process, when it is necessary to load and unload several Gigabytes of data at each step of the algorithm [38,39], This represents a significant system slowdown. Finally, PARREC follows an interactive policy, such to allow the user to control every step of data analysis.

Essential, for the success of the correction procedure, is the implementation of a 3D ray-tracing algorithm, needed to measure the thickness of the material crossed by the X-rays.

As previously anticipated, the amount of memory necessary to store the data is of the order of Gigabytes, such that a complete 3D ray-tracing will employ a too high computational time. Using 90° only is faster, but it requires that the object is positioned with its maximum thickness parallel to the detector plane, otherwise a 180° ray-tracing option is also possible (see Fig. 8). This reduced volume portion limits the execution time and, at the same time, provides ten thousand of points spanning a wide range of thickness, usually enough for a comprehensive analysis of the object shape. To the best of our knowledge, it is the first time that this approach is employed for BHC of complex shaped objects.

Generally, the BHC has been performed following four main steps:

- the choice of the subset of data with which to retrieve the relation between r and A′(r) (CRS-only or volumetric);
- the segmentation of the object from the background (using well known segmentation procedures);
- the choice of the model for the BHC;
- the correction and the reconstruction.

Finally, the corrections and the reconstructions have been achieved employing a Red-Hat virtual machine with Windows 11, 2 CPU AMD EPYC-Rome Processor, 12 cores and 24 logical processors, 24 tasks with hyperthreading, 64 GB RAM, 4 TB hard disk.

Using the previously described system, we achieved the reconstruction times indicated in Table 2.

Table 2
Data and processing times related to the reconstruction of the statue in Fig. 11 with a binning of 3 × 3.

Number of attenuated radiographs	900
Dimensions of a single attenuated radiograph (pixels)	879 × 1034
Dimensions of a single attenuated radiograph (MB)	3.46
Number of slices	879
Dimensions of a single slice (pixels)	879 × 1034
Time for ray-tracing (s)	27
Time for correction of all attenuated radiographs (s)	129
Time for correction of a single attenuated radiograph (s)	0.17
Time for reconstruction of all slices (s)	527
Time for reconstruction of a single slice (s)	0.6

3. Experiments

3.1. Experimental setup

Two groups of samples have been employed to perform experimental tests.

To the first one the scans of two aluminium cylinders of 1 cm and 3

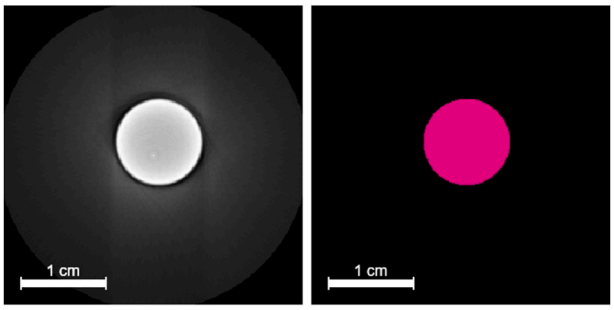

Fig. 9. Top views of the segmentation of the 1 cm diameter cylinder. On the left, the reconstructed central slice (before the BHC); on the right, the result of the segmentation.

cm diameters belong: they have been acquired at the CT laboratories of the Department of Physics and Astronomy of Bologna University. We used an operational X-ray tube voltage (industrial liquid cooled Bosello XRG120IT, focal spot 0.8 IEC) of 70 kV and a current of 2.7 mA. A Varian PaxScan 2520D indirect conversion flat-panel (1536 × 1920 pixels, size 127 μm) was employed as the detector. We acquired 900 angles for each section. The Source-Detector Distance (SDD) was measured to be 1216 mm and the Source-Object Distance (SOD) was equal to 1027 mm. Those parameters resulted in a magnification ratio of 1.184 and a final voxel size of 107.26 μm. The CRS was measured to be at line number 990 of the detector.

The second group consists of two Canova's clay sketches preserved at the Museo Gypsotheca "Antonio Canova", located in Possagno, Italy: the scans have been performed with a portable equipment, mounted directly in the museum. The used setup consisted in a portable Comet X-ray tube, model EVO 200D, and the same flat-panel detector described above.

After the assembling, the SDD was measured to be 1398 mm and the SOD was equal to 1188.5 mm, with a consequent magnification ratio of 1.176 and a final voxel size of 108 μm.

The scan has been operated with an X-ray tube voltage of 170 kV, 3 mA current, with a 1 mm steel filter. Being the scanned object bigger than the detector field of view (FOV), the tile scanning technique has been used (this technique involves the division of the scanned object in different sections, performing a separate scan for each one of them, and grouping them together before the reconstruction [40]). After the alignment, the position of the CRS plane was measured to be at line number 411 of the detector.

3.2. Experimental results

Experimentally, the two groups of samples have been used to test the efficacy of the proposed method and its implementation.

For the first group, including a couple of aluminium cylinders, of diameter 1 cm and 3 cm, a CRS analysis has been compared with a 3D ray-tracing one. An example of the segmentation of the central slice is shown in Fig. 9.

In this phase, we want to compare the behaviour of the fitting when using only the CRS or a complete 3D ray-tracing, in absence of central symmetry.

The profiles of the corrected values, for a single slice, are shown in Fig. 10. In these simple geometrical cases, the results achieved by the two different approaches are similar, confirming they both work correctly, with a small improvement in the 3D ray-tracing case.

The scans for the second group of samples have been acquired during the same measurement campaign, therefore with the same system parameters.

The first sketch mainly develops vertically, the CRS falling around

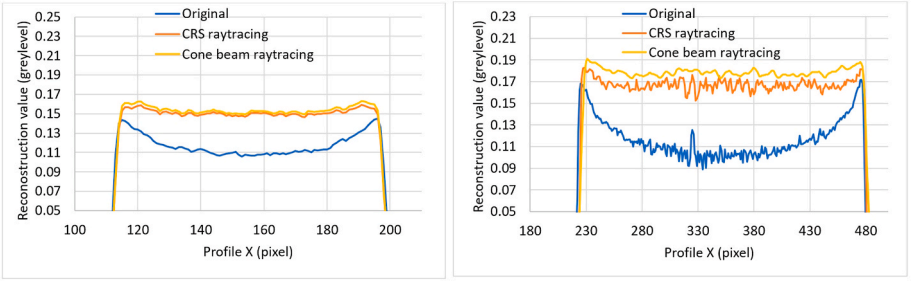

Fig. 10. Reconstruction profiles for a single slice from the 1 cm (left) and 3 cm (right) diameter cylinders. In blue the original data, in orange the BHC using the CRS approach, in yellow the BHC using the 3D ray-tracing: both provide similar results, with a slightly increased contrast in case of the mixed model. In this case, being the magnification of both cylinders close to one, the CRS with a polynomial approximation is suitable for the BHC and both models provide similar results.

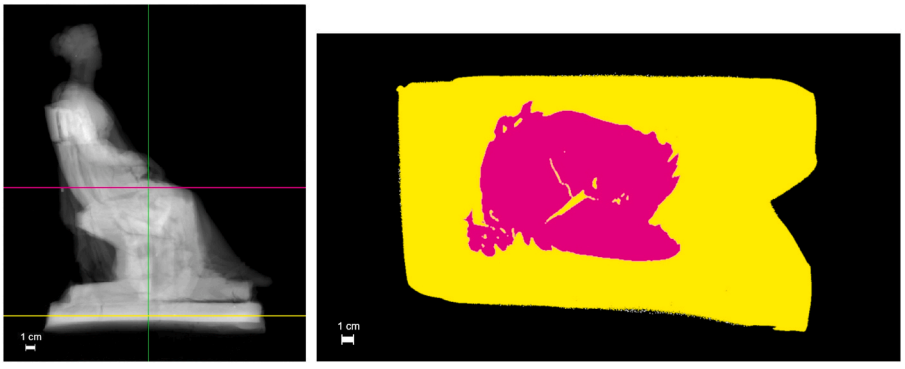

Fig. 11. (a) An attenuated radiograph with the indication of the center of rotation of the scanning system, individuated by the intersections of the green and the magenta lines. (b) Segmentation of the CRS (in magenta) over the basement (in yellow), view from top. The reference lines for the segmentation are indicated in (a) with the respective colours. The size of the CRS is reduced if compared with the dimensions of the basement, such that its single analysis is not suitable for the BHC. (a) An attenuated radiograph of the first Canova's sketch (b) Segmentation.

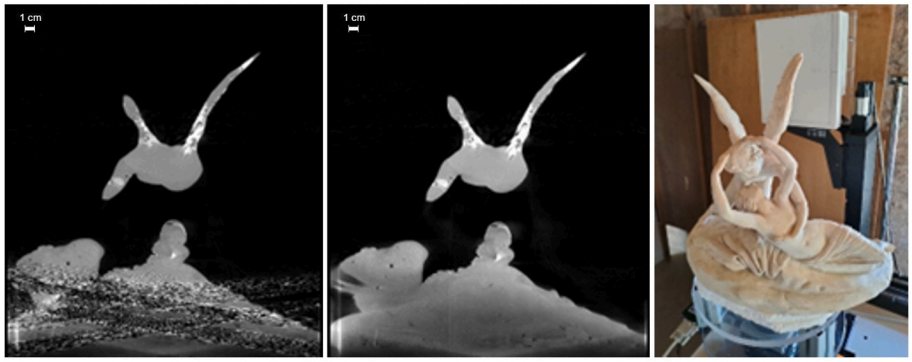

Fig. 12. an example of ineffective BHC of one Canova's sketch using polynomial approximation (4th order). The black and white points in the basement of the sketch are the result of the saturation corrupting the final reconstruction, described in Fig. 4. For comparison, the reconstruction achieved using our new model is shown in (b). In (c) the real image of the analysed sketch (image courtesy of the Museo Gypsotheca "Antonio Canova", Possagno, Italy).

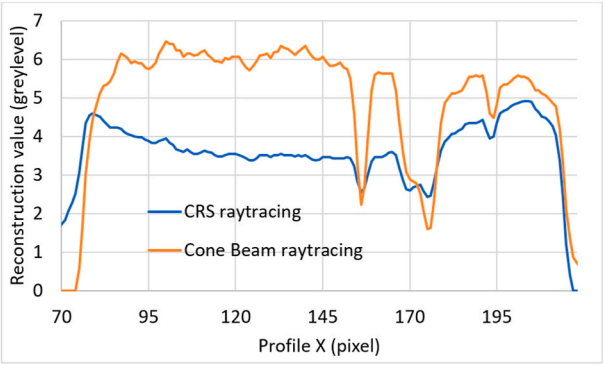

Fig. 13. Plot of the grey levels after the reconstruction achieved with CRS-P (blue) and VRT-M (orange). The reconstruction achieved by using the mixed model exhibits an improved contrast.

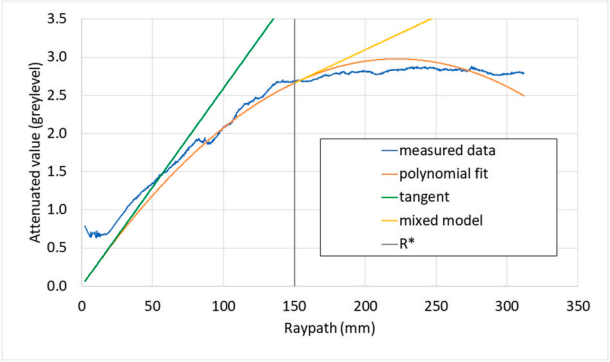

Fig. 14. Experimental trend of the polynomial fitting (orange), given the measured data (in blue). The green line is the tangent to the 2nd order polynomial fit. The vertical grey line individuates R*. The yellow line is the tangent to the polynomial in the mixed model, thanks to which the overcorrection is avoided.

one half of the height of the manufact (see Fig. 11).

In Fig. 12, two examples of reconstruction employing the method proposed in Ref. [26] are shown. It is evident how the saturation corrupts the final reconstructions.

Initially, we compared the profiles of the reconstructions achieved by using two different algorithms: the CRS analysis together with the polynomial model (CRS-P), and the volumetric ray-tracing combined with the mixed model (VRT-M), described by eq. (4) and eq. (6). The results, shown in Fig. 13, exhibit a better correction of our proposed

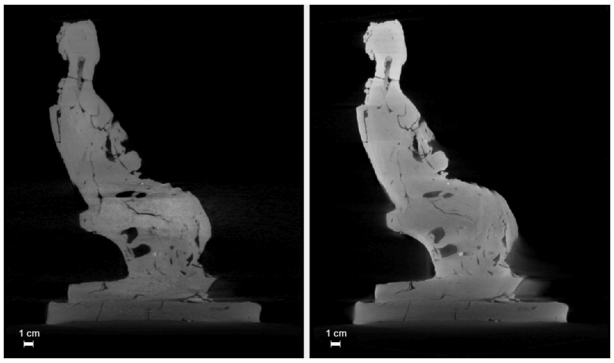

Fig. 15. A single slice reconstruction with (a) and without (b) the mixed model BHC. The corrected figure on the left exhibits more uniformity with a higher contrast, as shown in Table 1.

model, compared with the standard CRS-P.

Moreover, we verified that the second order polynomial approximation is actually affected by over correction, confirmed by the experimental trend shown in Fig. 14: on the other hand, the fitting of the mixed model avoids this effect.

An example of a reconstructed slice with and without the BHC with the proposed method is provided in Fig. 15.

The last example consists of the challenging BHC of another clay sketch by Canova. In this case, due to positioning problems, the CRS of the object belongs to a slice not meaningful for the BHC. Our proposed method, working on the whole volume of the object, is able to achieve an effective BHC also in this particularly difficult case, in which the sketch is asymmetric, its thickness is varying and the CRS is positioned at a level for which the data are far to be representative of the whole volume (see Fig. 16).

The missing consideration of an appropriate subset of thickness values would give rise to the impossibility to manage the BHC for most points in the data (see Fig. 17).

This lack depends on the not monotonic trend of the polynomial function, given that the central slice is not fully representative of the whole object. To overcome this limitation, we perform the 3D ray-tracing process.

The corrections are shown, again, in Fig. 14: the grey vertical line represents the value of R*, after which the linear model is considered.

In general cases, due to the variability of the data, it is not possible to state a priori what is the best value for R*. Thanks to the reduced execution time, subsequent reconstructions are possible: they are useful to experimentally determine a suitable value for R*. In Fig. 19 the final reconstruction is presented, while in Fig. 20 the comparison between two grey level profiles for a single corrected and not corrected slice is

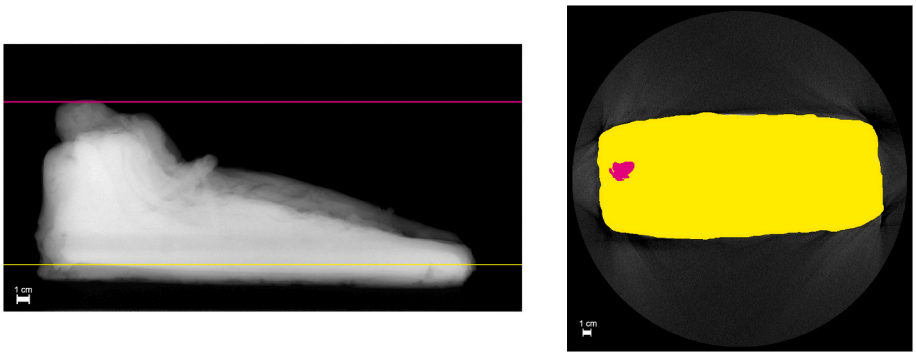

Fig. 16. Segmentation of the central slice of the Canova's sketch. (a) The purple line highlights the height of the central slice on one single attenuated radiograph. On the same figure, the yellow line highlights the thicker base level. (b) The segmentation (in purple) of the CRS section, view from top. The yellow area represents the base of the draft, much larger than the CRS, that is therefore not representative.
(a) An attenuated radiograph of the second Canova's sketch. (b) Segmentation.

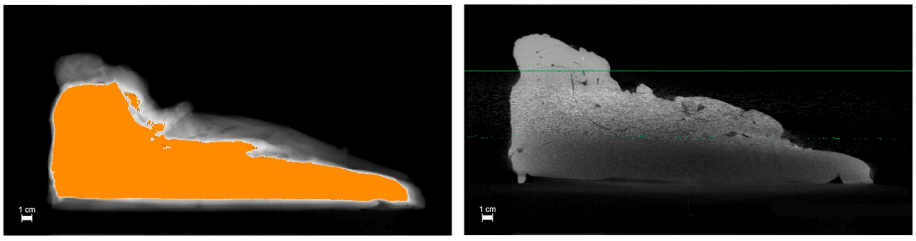

Fig. 17. On the left, highlighted in orange, in the middle of the object, the set of points that cannot be correctly managed without the introduction of a proper model. On the right, the reconstruction using the second order polynomial model.

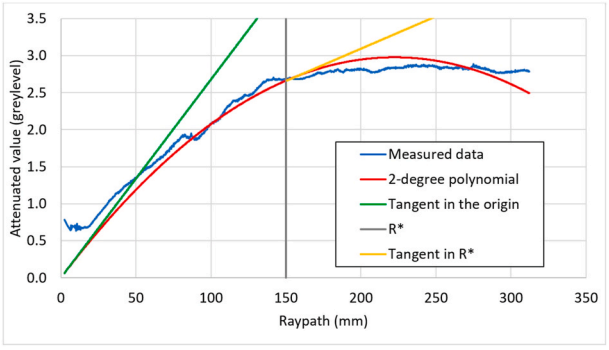

Fig. 18. Correction settings using the new model. The red line is the second order polynomial fit, operated on the measured data (in blue). Where the trend of the data changes (vertical grey line), the tangent to the polynomial is introduced (in green). The orange straight line represents the line compared to which the correction is operated.

shown.

For both the clay sketches, the contrast values, calculated according to Weber [41], are much higher in the corrected images than in the original ones, as shown in Table 3.

In addition, the grey level profiles, along a line crossing inner cavities in the objects, are shown in Fig. 21: the increased steepness of the profiles underlines a higher visual definition of the reconstructions after BHC.

Even if the new method has its own advantages, it is not possible anyway to correct too extreme situations, caused by the almost complete lack of an adequate signal level (e.g., in the basement of the sketch of Fig. 19).

4. Conclusions and final remarks

In real cases, to perform calibration-free and reliable BHC on objects with complex shapes and heterogeneous material, a model capable to manage the behaviour for high values of thickness, is needed. Generally, the polynomial fitting, due to its mathematical formulation and the lack

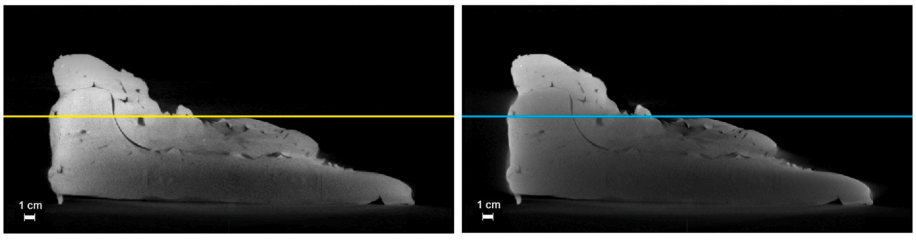

Fig. 19. (a) A single slice of the reconstruction of the Canova's clay sketch, using the correction parameters of Fig. 18. (b) The reconstruction of the data without the BHC. Visually improvements are evident. In particular: the border lines are much more well delineated, on the borders of the object, and internally in the holes of the material. The blurring effect, present in the Fig. 19b) and resulting in a visual resolution loss, is reduced by the BHC. The bottom part of the object remains practically unchanged, missing a set of consistent attenuation data.
(a) Reconstruction with BHC. (b) Reconstruction without BHC.

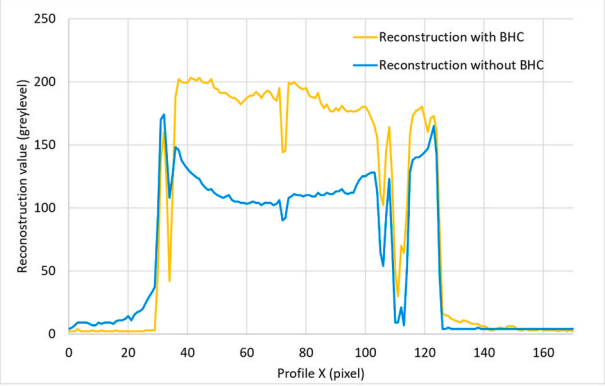

Figure 20. Curves of the grey levels for a single reconstruction before the BHC (cyan line) and after it (yellow line). The profiles refer to the respective yellow and cyan lines plotted at the heights highlighted in Fig. 19. An improvement of the contrast, after the BHC, is evident.

Table 3
Weber contrast for the two Canova's sketches. After the BHC the contrast is considerably increased.

Sketch nr.	Original contrast	BHC contrast
1	0.92 ± 0.17	5.25 ± 0.21
2	0.55 ± 0.17	4.95 ± 0.29

of a complete set of back-projected data, exhibits a not monotonicity that not correctly describes the attenuation phenomenon. To compensate this lack, we extended an existing method for calibration-free BHC, introducing a new model, justified from a theoretical perspective and proven to be effective from the applications point of view.

Moreover, for those cases when the CRS is not representative of the different values of the thicknesses in the object, we implemented a 3D ray-tracing procedure, to correct for higher values of r.

The new method has shown practical advantages in applications, and it has been validated on complex CH manufacts scans.

In particular, we proved the new model avoids over corrections and correctly manage otherwise "saturating" values, that normally cause artifacts and saturation in the 3D final reconstructions.

We implemented the model with a contained computational cost, that allows to apply it on big datasets, also of several Gigabytes: in this sense, the correction is effective for concrete real cases. To achieve these performances and reduce the execution time, further software algorithmic approximations have been introduced.

Like each experimental method, the new proposed one makes no claims of absolute effectiveness and is subject to uncertainty. However, it allows for adaptable fast post-correction tailored to each specific case. We assume that the object is primarily composed of the same material and apply this method exclusively to cases where the composition is primarily attributed to a single material. In the specific example of Canova's sketches, terracotta and plaster are evidently the predominant materials in the artwork.

Anyway, in line of principle, it is possible to think to extend our proposed methodology to multi-material cases by using image processing algorithms for the segmentation of uniform or quite-uniform areas. In those cases, the BHC would be locally applied for each segmented zone. The level of difficulties for the implementation of the solution for such a multi-dimensional problem could be the object for future researches.

Thanks to its parametric nature and to the software implementation, in which the parameters can be easily set by the user, the proposed methodology is suitable to perform multiple tests in a contained time, allowing to choose the best solution case by case. This fact makes it versatile and particularly suitable, but not limited, for Cultural Heritage measurement campaigns.

CRediT authorship contribution statement

Marco Seracini: Writing – review & editing, Writing – original draft, Visualization, Validation, Methodology, Investigation, Formal analysis, Data curation. **Matteo Bettuzzi:** Writing – review & editing, Visualization, Validation, Methodology, Investigation, Data curation, Conceptualization, Formal analysis. **Rosa Brancaccio:** Writing – review & editing, Writing – original draft, Validation, Software, Methodology, Investigation, Formal analysis, Data curation, Conceptualization, Visualization. **Maria Pia Morigi:** Writing – review & editing, Supervision,

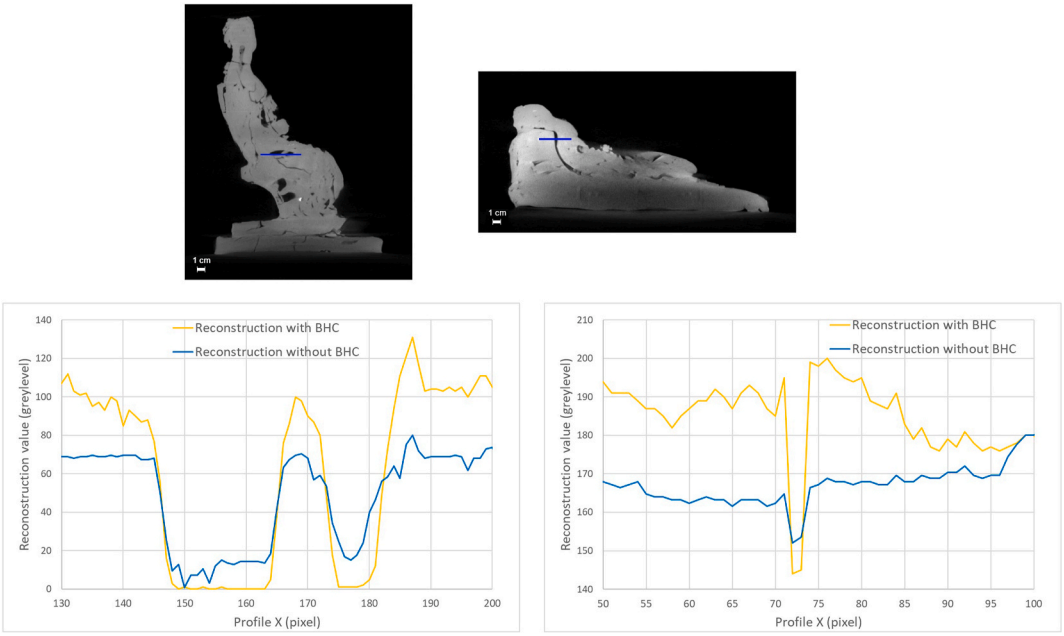

Fig. 21. Under the image of each clay sketch, its grey level profile, for the highlighted blue line. In the graphs, in blue the trend for the not corrected reconstruction; in yellow the trend after the BHC. The higher steepness of the curves when crossing the holes puts in evidence the advantage achieved after the BHC.

Project administration.

Declaration of competing interest

The authors declare that they have no known competing financial interests or personal relationships that could have appeared to influence the work reported in this paper.

Data availability

Data will be made available on request.

References

[1] F. Stanco, S. Battiato, G. Gallo (Eds.), Digital Imaging for Cultural Heritage Preservation: Analysis, Restoration, and Reconstruction of Ancient Artworks, CRC press, 2017.

[2] X. Huang, E. Uffelman, O. Cossairt, M. Walton, A.K. Katsaggelos, Computational imaging for cultural heritage: recent developments in spectral imaging, 3-D surface measurement, image relighting, and X-ray mapping, IEEE Signal Process. Mag. 33 (5) (2016) 130–138.

[3] B. Borg, M. Dunn, A. Ang, C. Villis, The application of state-of-the-art technologies to support artwork conservation: literature review, J. Cult. Herit. 44 (2020) 239–259.

[4] S. Hermon, F. Niccolucci, N. Bakirtzis, S. Gasanova, A heritage digital twin ontology-based description of Giovanni Baronzio's "Crucifixion of Christ" analytical investigation, J. Cult. Herit. 66 (2024) 48–58, https://doi.org/10.1016/j.culher.2023.11.004.

[5] M. Slaney, A.C. Kak. *Principles of computerized tomographic imaging*, IEEE press, 1988.

[6] E. Van de Casteele, D. Van Dyck, J. Sijbers, E. Raman, An energy based beam hardening model in tomography, Phys. Med. Biol. 47 (23) (2002) 4181–4190, https://doi.org/10.1088/0031-9155/47/23/305.

[7] E. Van de Casteele, D. Van Dyck, J. Sijbers, E. Raman, The effect of beam hardening on resolution in x-ray microtomography, in: Proc. SPIE 5370, Medical Imaging 2004: Image Processing, 2004, https://doi.org/10.1117/12.535263.

[8] Peter M. Joseph, Robin D. Spital, A method for correcting bone induced artifacts in computed tomography scanners, J. Comput. Assist. Tomogr. 2 (1) (1978) 100–108.

[9] P. Rüegsegger, et al., Standardization of computed tomography images by means of a material-selective beam hardening correction, J. Comput. Assist. Tomogr. 2 (2) (1978) 184–188.

[10] M.B. Kiss, F.G. Bossema, P.J.C. van Laar, et al., Beam filtration for object-tailored X-ray CT of multi-material cultural heritage objects, Herit. Sci. 11 (2023) 130, https://doi.org/10.1186/s40494-023-00970-z.

[11] Peter K. Kijewski, Bengt E. Bjärngard, Correction for beam hardening in computed tomography, Med. Phys. 5 (3) (1978) 209–214.

[12] O. Nalcioglu, R.Y. Lou, Post-reconstruction method for beam hardening in computerised tomography, Phys. Med. Biol. 24 (2) (1979) 330.

[13] Dimeng Xia1, Shusen Zhao2, Huitao Zhang1,2, Yining Zhu1,2, Xing Zhao1,2 and Peng Zhang1, An iterative method for simultaneous reduction on beam-hardening and scatter artifacts in x-ray CT, Published 30 March 2023 © 2023 IOP Publishing Ltd, Physica Scripta, Volume vol. 98, Number 4 Citation Dimeng Xia et al 2023 Phys. Scr. 98 045230DOI 10.1088/1402-4896/acc61b.

[14] Gabor T. Herman, Sushma S. Trivedi, A comparative study of two post reconstruction beam hardening correction methods, IEEE Trans. Med. Imag. 2 (3) (1983) 128–135.

[15] Robertson Jr., D. Douglas, H.K. Huang, Quantitative bone measurements using x-ray computed tomography with second-order correction, Med. Phys. 13 (4) (1986) 474–479.

[16] J.M. Meagher, C.D. Mote, H.B. Skinner, CT image correction for beam hardening using simulated projection data, IEEE Trans. Nucl. Sci. 37 (4) (1990) 1520–1524.

[17] Peter M. Joseph, Christopher Ruth, A method for simultaneous correction of spectrum hardening artifacts in CT images containing both bone and iodine, Med. Phys. 24 (10) (1997) 1629–1634.

[18] Peter K. Kijewski, Bengt E. Bjärngard, Correction for beam hardening in computed tomography, Med. Phys. 5 (3) (1978) 209–214.

[19] Yiannis Kyriakou, Esther Meyer, Daniel Prell, Marc Kachelrieß, Empirical Beam Hardening Correction (EBHC) for CT, First published, 2010, https://doi.org/10.1118/1.3477088, 08 September.

[20] Analytical Methods Committee AMCTB No.98,, X-ray micro computed tomography in cultural heritage, Anal. Methods 12 (36) (2020) 4496–4500, https://doi.org/10.1039/d0ay90112a.

[21] O. Enguita, T. Calderón, M.T. Fernández-Jiménez, P. Beneitez, A. Millan, G. García, Damage induced by proton irradiation in carbonate based natural painting pigments, Nucl. Instrum. Methods Phys. Res. Sect. B Beam Interact. Mater. At. 219–220 (2004) 53–56.

[22] L. Cortella, C. Albino, Q.K. Tran, K. Froment, 50 years of French experience in using gamma rays as a tool for cultural heritage remedial conservation, Radiat. Phys. Chem. 171 (2020) 108726.

[23] W. Bras, H. Stanley, Unexpected effects in non crystalline materials exposed to X-ray radiation, J. Non-Cryst. Solids 451 (2016) 153–160.

[24] L. Bertrand, S. Schöeder, D. Anglos, M.B. Breese, K. Janssens, M. Moini, A. Simon, Mitigation strategies for radiation damage in the analysis of ancient materials, TrAC, Trends Anal. Chem. 66 (2015) 128–145.

[25] J. Levi, B.L. Eck, R. Fahmi, H. Wu, M. Vembar, A. Dhanantwari, A. Fares, H. G. Bezerra, D.L. Wilson, Calibration-free beam hardening correction for myocardial perfusion imaging using CT, Med. Phys. 46 (2019) 1648–1662, https://doi.org/10.1002/mp.13402.

[26] W. Zhao, G.T. Fu, C.L. Sun, Y.F. Wang, C.F. Wei, D.Q. Cao, J.M. Que, X. Tang, R. J. Shi, L. Wei, Z.Q. Yu, Beam hardening correction for a cone-beam CT system and its effect on spatial resolution, Chin. Phys. C 35 (10) (2011) 978–985, https://doi.org/10.1088/16741137/35/10/018.

[27] F. Di Turo, G. Moro, A. Artesani, et al., Chemical analysis and computed tomography of metallic inclusions in Roman glass to unveil ancient coloring methods, Sci. Rep. 11 (2021), https://doi.org/10.1038/s41598-021-90541-8, 11187.

[28] F. Albertin, M. Bettuzzi, R. Brancaccio, M.B. Toth, M. Baldan, M.P. Morigi, F. Casali, Inside the construction techniques of the Master globemaker Vincenzo Coronelli, Microchem. J. 158 (2020), https://doi.org/10.1016/j.microc.2020.105203, 105203.

[29] G.T. Herman, Correction for beam hardening in computed tomography, Phys. Med. Biol. 24 (1) (1979) 81–106, https://doi.org/10.1088/00319155/24/1/008.

[30] G.N. Hounsfield, The E.M.I. Scanner, Proc. R. Soc. Lond. Ser. B, Biol. Sci. 195 (1119) (1977) 281–289, https://doi.org/10.1098/rspb.1977.0008. . ISSN 0080-4649.

[31] N. Otsu, A threshold selection method from gray-level histograms, IEEE Trans. Syst., Man, Cybern. 9 (1) (1979) 62–66.

[32] J. Canny, A computational approach to edge detection, IEEE Trans. Pattern Anal. Mach. Intell., PAMI- 8 (6) (1986) 679–698, https://doi.org/10.1109/TPAMI.1986.4767851.

[33] R. Brancaccio, M. Bettuzzi, F. Casali, M.P. Morigi, G. Levi, A. Gallo, G. Marchetti, D. Schneberk, 3D tomographic reconstruction on HPC cluster of the Kongo Rikishi (Japanese wooden statue of the XIII century), real time conference (RT), conference record on CD-ROM 17th real-time conference, in: IEEE-NPSS Technical Committee on Computer Applications in Nuclear and Plasma Sciences, 2010, pp. 1–8. ISBN: 978-1-4244-7108-9.

[34] R. Brancaccio, M. Bettuzzi, F. Casali, M.P. Morigi, G. Levi, A. Gallo, G. Marchetti, D. Schneberk, Real-time reconstruction for 3-D CT applied to large objects of cultural heritage, IEEE Trans. Nucl. Sci. 58 (4) (2011) 1864–1871. ISSN: 0018-9499.

[35] R. Brancaccio, M. Bettuzzi, M.P. Morigi, F. Casali, L. Ragazzini, Image quality and dose assessment in inner ear computed tomography imaging with a flat panel-based system, J. Comput. Assist. Tomogr. 39 (2) (2015) 232–239, https://doi.org/10.1097/RCT.0000000000000176.

[36] E. Corni, M.P. Morigi, R. Brancaccio, M. Bettuzzi, G. Levi, E. Peccenini, L. Morganti, D. Cesini, A. Ferraro, X-Ray computed tomography applied to objects of cultural heritage: porting and testing the filtered back-projection reconstruction algorithm on low power systems-on-chip, in: Parallel, Distributed, and Network-Based Processing (PDP), 24th Euromicro International Conference on, IEEE. Electronic, 2016 369372. ISBN: 978-1-4673-8776-7 USB ISBN: 978-1-4673-8775-0 Electronic ISSN: 2377-5750.

[37] Method for the Interactive Parallel Processing of Data on a Cluster with the Graphic Input/output on a Visualisation Device", code: PCT/IT2013/000322.

[38] Y. Fujii, T. Azumi, N. Nishio, S. Kato, M. Edahiro, Data transfer matters for GPU computing, in: 2013 International Conference on Parallel and Distributed Systems, IEEE, 2013, December, pp. 275–282.

[39] S. Pal, S. Feng, D.H. Park, S. Kim, A. Amarnath, C.S. Yang, R. Dreslinski, Transmuter: bridging the efficiency gap using memory and dataflow reconfiguration, in: Proceedings of the ACM International Conference on Parallel Architectures and Compilation Techniques, 2020, September, pp. 175–190.

[40] M.P. Morigi, F. Casali, M. Bettuzzi, et al., Application of X-ray computed tomography to cultural heritage diagnostics, Appl. Phys. A 100 (2010) 653–661, https://doi.org/10.1007/s00339-010-5648-6.

[41] E. Peli, Contrast in complex images, J. Opt. Soc. Am. A 7 (10) (1990) 2032–2040, https://doi.org/10.1364/JOSAA.7.002032.